SANDIA REPORT

SAND 2002-8076
Unlimited Release
Printed February 2002

SELF-ASSEMBLED TEMPLATES FOR FABRICATING NOVEL NANO-ARRAYS AND CONTROLLING MATERIALS GROWTH

R.Q. Hwang, C.S. Ashley, C.J. Brinker, C.C. Mitchell, M.E. Bartram & M.E. Coltrin

Prepared by
Sandia National Laboratories
Albuquerque, New Mexico 87185 and Livermore, California 94550

Sandia is a multiprogram laboratory operated by Sandia Corporation, a Lockheed Martin Company, for the United States Department of Energy under Contract DE-AC04-94AL85000.

Issued by Sandia National Laboratories, operated for the United States Department of Energy by Sandia Corporation.

Available to DOE and DOE contractors from
U. S. Department of Energy
Office of Scientific and Technical Information
P.O. Box 62
Oak Ridge, TN 37831

Telephone: (865)576-8401
Facsimile: (865)756-5728
E-Mail:reports@adonis.osti.gov
Online ordering: http://www.doe.gov/bridge

Available to the public from
U. S. Department of Commerce
National Technical Information Service
5285 Port Royal Rd
Springfield, VA 22161

Telephone: (800)553-6847
Facsimile: (703)605-6900
E-Mail:orders@ntis.fedworld.gov
Online order: http://www.ntis.gov/ordering.htm

SAND 2002-8076
Unlimited Release
Printed February 2002

SELF-ASSEMBLED TEMPLATES FOR FABRICATING NOVEL NANO-ARRAYS AND CONTROLLING MATERIALS GROWTH

R.Q. Hwang
Surface and Interface Science Department
Sandia National Laboratories
Livermore, CA 94551

C.S. Ashley, C.J. Brinker
Materials Chemistry Department

C.C. Mitchell, M.E. Bartram and M.E. Coltrin
Chemical Processing Science Department
Sandia National Laboratories
Albuquerque, NM 87185-0601

ABSTRACT

Novel and exciting phenomena which have the potential to revolutionize science, materials, next-generation production methods are manifested as structural dimensions approach the nanometer level. However, advances in lithography are insufficient to achieve this feature scale. As a result, molecular self-assembly has attracted a great deal of interest, since this provides a possible spontaneous mechanism by which nanometer sized arrays can be formed without mechanical intervention. Although these "low tech" processes are highly dependent on system/material specifics, we propose that new techniques and the science which underlies them can be developed in a manner that allows us to extend the natural order of self-assembling systems. The approach we will employ is based on previous work in which we fabricated templates of unprecedented size and regularity. These templates will then be applied to form nano-arrays based on a wide range of materials with tunable properties and nano-scale selective area over-growth patterns for improving the materials quality of thin films.

This page intentionally left blank

Contents

Page

Title Page……..3

I. Self-Assembled Nanoscale Templates in Strained Metal Films…….....5

II. Evaporation-Induced Self-Assembly EISA)..……...17

III. Kinetics and Transport in Gallium Nitride Epitaxial Lateral Overgrowth and its Application to Sol-Gel Based SI102 Films.…….25

Distribution……..……...33

This page intentionally left blank

SELF-ASSEMBLED TEMPLATES FOR FABRICATING NOVEL NANO-ARRAYS AND CONTROLLING MATERIALS GROWTH

I. SELF-ASSEMBLED NANOSCALE TEMPLATES IN STRAINED METAL FILMS

Natural nanoscale processes can create ordered structures that rival our most advanced patterning technologies[1,2]. Though many observations of self-organization have been reported[1-15], the fundamental mechanisms underlying such behavior are not well characterized. In particular, the nature of the forces leading to and stabilizing self-organized behavior is not well understood. In part, this is due to the fact that the forces between the many-atom individual units in these structures, with characteristic lengths of 10's to 100's of ångstroms, must extend far beyond the range that is typical for direct interactions between single atoms. A commonly accepted source of such mesoscopic-scale forces is the surface stress field mediated by the substrate, which supports the grown structures. This, however, has not been confirmed, nor have such interactions been directly measured.

Here, we address these issues with a new approach: We monitor an array of nano-structures as a function of time so as to quantify the influence of the individual units of the array on each other's positions, thereby probing the strength and physical origin of the underlying interactions. Specifically, we apply time-resolved scanning tunneling microscopy (STM) to track the thermal motion of a two-dimensional (2D) lattice of vacancy islands which forms upon exposure of a single atomic layer of Ag on Ru(0001) to sulfur, at room temperature. These islands vibrate around their equilibrium positions in a manner similar to atomic vibrations, or phonons, in a crystal. A normal mode analysis of the vibrations obtains the elastic constants of the lattice, which we relate to general theories of elastically mediated interactions between surface defects in strained films. There have been no comparable studies of lattice dynamics in real 2D crystals[16-18].

Monitoring The Self-Assembly Of The Island Array

We start by describing the experimental procedure by which we are able to create the array of vacancy islands in our Ag film. First, a clean Ru(0001) surface was prepared in ultrahigh vacuum. Slightly under one monolayer (ML) of Ag was then deposited onto this surface, at room temperature. A Ag film forms which is highly strained as a result of the lattice mismatch between Ag and Ru (the native bond length of Ag being about 7% larger than that of Ru). A flash anneal to 750 K, to obtain an equilibrium surface, one single layer high, invariably produces an ordered pattern in the Ag adlayer (unit cell~40×60Å), consisting of a near-square array of threading dislocations[19,20]. Subsequent exposure of this strained layer to sulfur, at room temperature, triggers surprisingly complex behavior in the Ag film. We studied three main regimes, distinguished by the sulfur coverage.

In the first stages of sulfur exposure, sulfur reacts with the film, displacing Ag atoms. What we see in the STM images are far-separated 2D vacancy islands of highly regular size, about 34±11 Å in diameter. These can be seen in Figure 1 (a, b). Sulfur in turn is found coating exposed Ru regions, including the inside of the islands, where it forms ordered 2D clusters; see the inset in Figure 1b**.** This is not surprising since the interaction between sulfur and Ru is stronger than that between sulfur and Ag, and it certainly reduces the energy cost of exposing the Ru(0001) surface by decreasing its surface energy. The isolated vacancy islands are extremely mobile, significantly more than has been reported for vacancy islands of similar size on clean metal (111) surfaces[21-23]. The motion of the island step edges is so rapid (much faster than the rate of STM image acquisition) that they have a "blurred" appearance; see Figure 1 (a, b). By using the STM to monitor the position of isolated islands as a function of time, we measured hop rates of several hundreds of ångstroms per minute at room temperature[24]. This high island mobility suggests that these structures are equilibrated. As we monitor this "dilute gas" of islands, we observe random formation (and dissociation) of small nearest-neighbor clusters of islands, separated by about 50 Å; see Figure 1 (a, b). Strong short-range repulsions between islands seem to prevent them from coalescing or from coming closer to one another.

The effect of these repulsions becomes increasingly dramatic as we add more sulfur, and the density of vacancy islands increases. The order of "crystalline" regions, whose assembly began in the low island density sequence of Figure 1 (a, b) becomes longer ranged. Near 0.1 ML of sulfur, a stable triangular lattice of vacancy islands forms, with a period of about 53 Å. The high degree of regularity of this lattice can be seen in Figure 1c. The distribution of vacancy island diameters is extremely narrow (±4 Å), and peaked at 24 Å. This impressive degree of order extends over each of the micron-wide terraces of the Ru(0001) surface, providing a striking new example of a self-ordered mesoscopic structure.

One hypothesis about the cause of the spontaneous formation of this periodic lattice of vacancy islands is that they are stabilized by long-range interactions, due to the stress field around each island associated with elastic relaxations of island step edges[1,25-27]. It has been shown that this leads to interactions between step edges, inversely proportional to their separation, and analogous to those between domain walls in electrostatic dipole systems[1,25,26]. The key question is whether this hypothesis and the nature of these interactions are consistent with our experimental data.

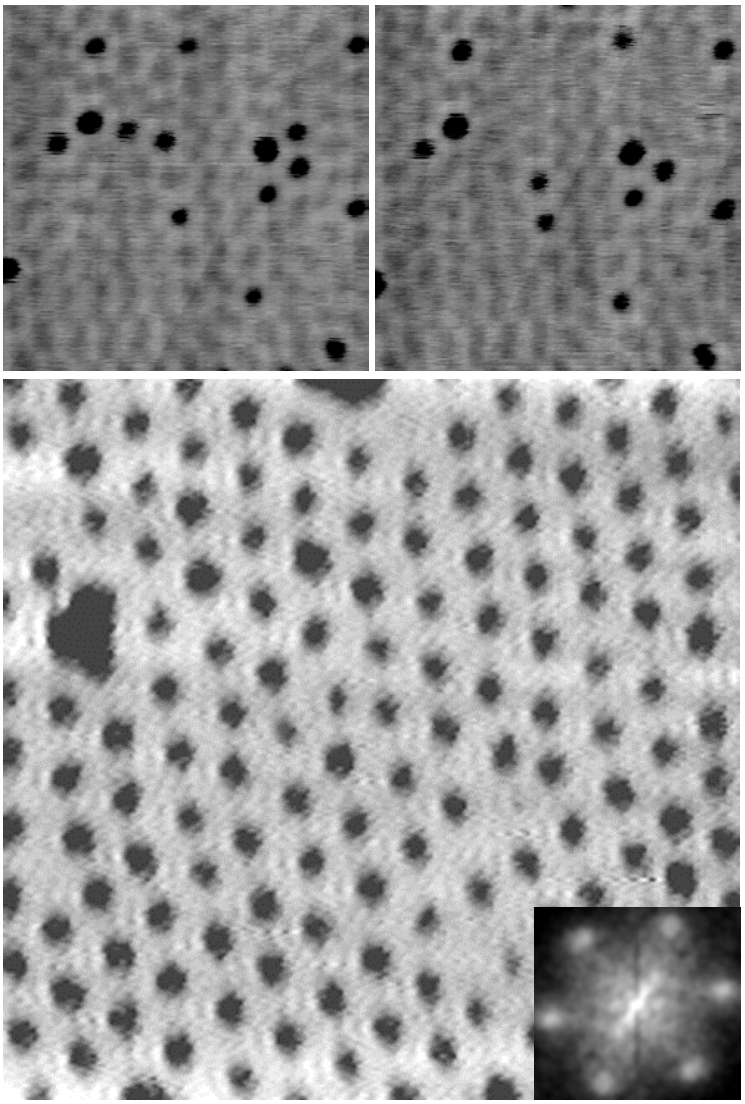

Figure 1. Low- and high-density vacancy island arrays. **(a-b)** Two frames, 2 minutes apart, of an STM movie of the same 480×480 $Å^2$ area of sulfur-exposed Ag/Ru(0001). The sulfur coverage is $\theta_S \approx 0.04$ ML, and the area fraction of vacancy islands is $f \approx 0.07$. Features reminiscent of the dislocation structure in the clean Ag film are still noticeable. The inset in **(b)** shows a 60×60 $Å^2$ STM image of a large vacancy island. (These are immobile compared to the smaller islands, but "breathe" on the time scale of image acquisition.) Inside the island is a cluster of sulfur atoms. Diffusing single vacancies are often observed in such clusters, disappearing at the island edge within minutes. **(c)** 600×600 $Å^2$ STM image of the vacancy island crystal. Here, $\theta_S \approx 0.1$ ML and $f \approx 0.2$. Defects in the crystal include large islands (density~2×10^{-5} $Å^{-2}$) and paired dislocation lines (density~7×10^{-6} $Å^{-2}$). The inset shows the Fourier transform of a 200×200 nm^2 image.

Measuring The Forces That Stabilize The Array

To answer this question, we exploit a remarkable observation from a large series of consecutive STM images of the vacancy island lattice. The islands perform thermal vibrations about their equilibrium positions, with clear traces of the high island mobility and probably occurring by the same mechanisms of island motion which were apparent in the low island density regime. This motion can be seen in the image overlay of Figure 2a. Quantitative analysis of these vibrations allows direct assessment of the strength of the interactions between neighboring islands.

We begin this analysis by following the displacement of the CM of each island in a 450×450 Å^2 array (about 80 islands) with time-resolved STM, recording images of the same area at 10-20 second intervals, for nearly 4 hours. To quantify this motion, we measured the CM displacement at time t for each island, defined as $\mathbf{u}(\mathbf{r_0},t)=\mathbf{r}(t)-\mathbf{r}_0$, where $\mathbf{r}(t)$ is the position of the CM at time t of the vacancy island at the equilibrium CM position $\mathbf{r_0}$. The typical range of values for the components of **u**, obtained by marking the CM trajectories over the complete data set, is shown for one island in Figure 2b. The motion of individual islands is correlated, reflecting the interactions between neighboring islands, as confirmed by measuring time correlations in the values of **u** for pairs of islands along the data set. Figure 2c shows clearly that **u**-values are positively correlated for neighboring islands, with correlation decaying rapidly with island-island separation.

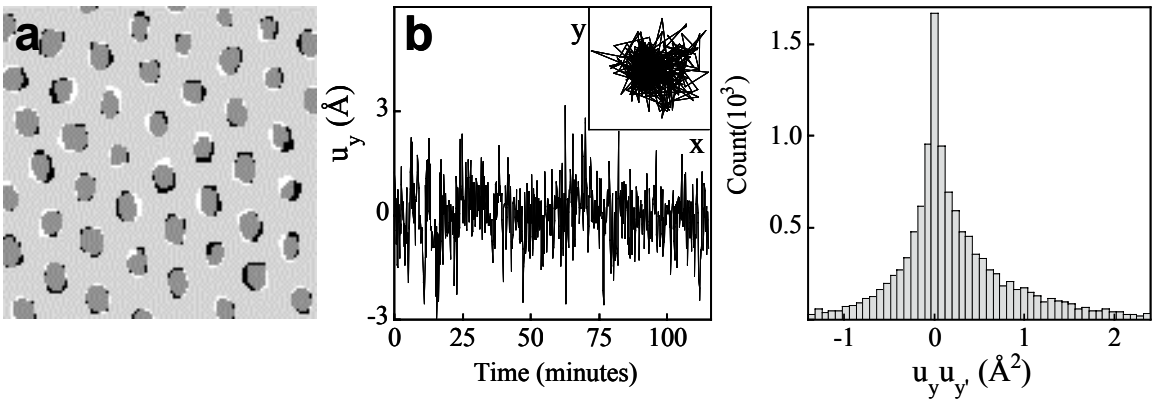

Figure 2. Phonons in the vacancy island crystal. **(a)** Overlay of two 300×300 Å^2 (contrast enhanced) images, 20 s apart, from an STM movie of the island lattice vibrations. In one of the frames the islands are black, in the other white (so the overlap is dark gray). **(b)** The y-component of the CM displacement of a selected island versus time, taken from a sequence of 690 frames, 10 s apart. The inset shows the full x-y trajectory for this island. **(c)** Distribution of the (equal-time) product of y-components, u_y and $u_{y'}$, of CM displacements of nearest-neighbor islands, over the 690 frames. The average is $\langle u_y u_{y'}\rangle \approx 0.26$Å^2. Skewness, $\kappa \approx 1.8$, in this distribution reflects (positive) correlation in the motion of nearest-neighbor islands. This correlation decreases rapidly with island-island separation: $\langle u_y u_{y'}\rangle \approx 0.1$, 0.07, <0.06 Å^2, and $\kappa \approx 0.9$, 0.6, <0.08, for pairs of islands separated by 2, 3, and >4 nearest-neighbor distances, respectively.

To analyze this correlated motion, we use the Fourier transformed displacements. This has a significant computational advantage: Since the displacement of the islands from their equilibrium lattice positions is small, we expect the vibrations in these positions to be well described as vibrations in a harmonic crystal. In this case, each Fourier component is expected to fluctuate independently, while satisfying equipartion of energy, thus allowing a simple connection between the measured amplitude of the thermal vibrations and the elastic constants of the crystal[28,29]. This is analogous to the way in which elastic properties are extracted from phonons in crystalline solids. We focus here on the long-wavelength behavior of the expectation value of the steady-state pair correlation function, defined as $G_{ij}(\mathbf{q})=(1/A)[\hat{u}_i(\mathbf{q})\hat{u}_j(-\mathbf{q})]$, between components i and j of the Fourier transformed displacements, $\hat{\mathbf{u}}(\mathbf{q})=\int d^2\mathbf{r_0}\ \mathbf{u}(\mathbf{r_0})\exp(i\mathbf{q}\cdot\mathbf{r_0})$. Here, A is the system area. These correlations are important because they provide a direct connection to the elastic properties of the vacancy lattice, as follows. The components i and j of $\hat{\mathbf{u}}(\mathbf{q})$ can equivalently be distinguished as components which are longitudinal (ℓ) or transverse (t) to $\mathbf{q}$. For small, non-zero $q=|\mathbf{q}|$, equipartion of energy amongst the independent modes then gives $G_{tt}(\mathbf{q})=k_BT/(q^2\mu)$ and $G_{\ell\ell}(\mathbf{q})=[k_BT/(q^2\mu)][1-(\lambda+\mu)/(\lambda+2\mu)]$, where T is the temperature, k_B is the Boltzmann constant, and λ and μ are the elastic Lamé coefficients of the lattice[28,29]. Specifically, the combination $\lambda+\mu$ measures changes in the elastic energy density[25,26] due to isotropic strain, whereas μ governs shear at constant unit-cell volume. By analyzing either the slopes of G_{tt} and $G_{\ell\ell}$ versus $1/q^2$, or the actual values of G_{tt} and $G_{\ell\ell}$ at some (small) $\mathbf{q}$, estimates of λ and μ can be obtained.

We choose to focus on a "perfectly" ordered 6×6 vacancy island cell, and analyze results for small q values. Figure 3 shows that the amplitude of $G_{\ell\ell}$ decreases rapidly with q, qualitatively as predicted. From these, and similar data for G_{tt}, we measured average values of $G_{\ell\ell}\approx 3\pm 1\text{nm}^4$ and $G_{tt}\approx 4\pm 2\text{nm}^4$, for $q=4\pi/(10\sqrt{3}\,b)\approx 0.14/\text{nm}$. Thus, we estimate $\lambda/c\approx\mu/c\approx 5\times10^7\text{-}10^8\ \text{N/m}^2$, consistent with values obtained from the width of the Gaussian distribution of mean square displacements, or from analysis of the shape and skewness of the distribution of displacement correlations for nearest-neighbor islands, in Figure 3. Here, c≈4 Å is the vertical lattice spacing of the Ag/Ru(0001) film, and is introduced to facilitate comparison with values for bulk elastic constants. Common values for these in ordinary bulk crystals, $\lambda_{bulk}\approx 10^{11}\text{N/m}^2$ and $\mu_{bulk}\approx 10^{10}\text{N/m}^2$, are 3-4 orders of magnitude larger, reflecting the fact that elastic interactions are typically substantially weaker than direct interatomic forces.

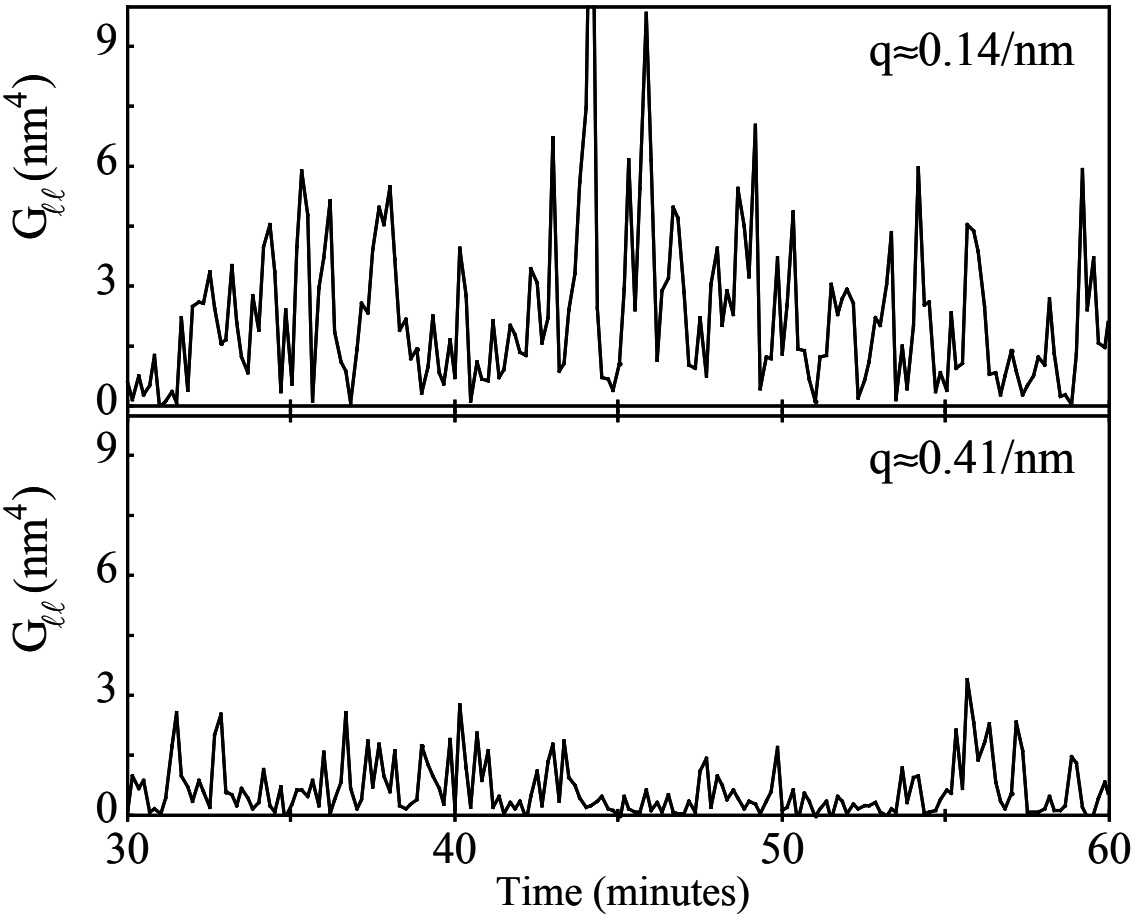

Figure 3. Analysis of correlations in the thermal displacements of neighboring islands. The time dependence of $G_{\ell\ell}q$) is shown for q≈0.14 and 0.41/nm, over 200 STM frames (about 1 hour). The average values are about 3 and 0.7 nm^4 (with larger uncertainty in the latter), for q≈0.14 and 0.41/nm, respectively.

A Model For The Elastic Coupling Between Islands

In order to test if stress field interactions indeed control the stability of these arrays of islands, explaining the order of magnitude of the elastic constants, one must examine how such interactions manifest themselves in our system. The most basic model that describes the elastic coupling between the vacancy islands includes two competing contributions to the total energy of the island array[25,26]. One is from the line tension, γ_b, which is the energy per unit length of the vacancy island edges. It expresses the cost of reducing the local coordination of atoms at island edges, and favors the formation of few, large, and far-separated islands (for a fixed area fraction of vacancies). To counter this tendency, there are elastic interactions, γ_d, between step edges of neighboring islands. These derive from the elastic deformation of atom positions near the edge of a step, associated with the tendency for undercoordinated atoms to adjust the bonds with their neighbors so as to increase their effective coordination and relax strain. (In the case of Ag, which has larger lattice constant than Ru, a slight outward expansion at the step edge is expected.) These elastic forces are repulsive for neighboring steps of adjacent islands, but attractive for like steps (weaker entropic and elastic dipole repulsions being neglected)[27]. The net contribution to the elastic energy, relative to that of a uniform film, is negative, thus favoring spontaneous vacancy island formation[1,25,26,30].

The first test of this model is whether it predicts the ordered triangular arrangement of vacancy islands. It does at sufficiently low area fraction of the film, f, occupied by vacancy islands. The complete phase diagram has been precisely computed numerically in ref 26. It predicts the existence of a critical fraction, $f_c \approx 0.29$, such that for $f \lesssim f_c$, the lowest energy structure is a triangular lattice of near-circular vacancy islands of narrowly-distributed radius and repeat distance; other lattice symmetries are possible, e.g., imposed by the substrate[15]. This is in qualitative agreement with our observation of a highly ordered vacancy island lattice in Figure 1. For $0.29 \lesssim f \lesssim 0.71$, an array of stripes, instead, is predicted by the model to have lower energy. To test the existence of this second ordered structure of stripes, we increased the sulfur coverage (which is equivalent to increasing f). Indeed, this produced a dramatic rearrangement of the surface into a pattern of double-layer Ag stripes (3.5-4 Å high), with a characteristic width and periodicity of 200-300 Å; see Figure 4**.** We have not confirmed that this is an equilibrium structure, nor have we yet pinpointed in our system the location, f_c, of the transition from the 2D crystal of vacancy islands to this striped phase, but the rough agreement with the predicted phase diagram is encouraging.

To more rigorously test the notion that elastic interactions are the stabilizing forces in the array of vacancy islands (and that of the stripes), we need to estimate the value of γ_d, and compare it to known ranges of these interactions for such systems. To extract such an estimate, we use the connection between γ_d and the elastic constants of the lattice obtained above from analysis of the thermal vibrations of the vacancy island lattice. Specifically, we find $\gamma_d = 3^{1/2}(\lambda+\mu)b^2/(\pi R)$, at constant f, where R is the average island radius, b is the island lattice repeat distance, and λ and μ are the Lamé coefficients described above (see K. Pohl *et al.,* in preparation). For our estimates of λ and μ, we find $\gamma_d \approx 0.15$-0.3 eV/Å, using $b \approx 53$ Å and $R \approx 12$ Å. γ_b is presumably of the order of magnitude of the line tension for Ag(111), roughly 0.1 eV/Å (ref 31).

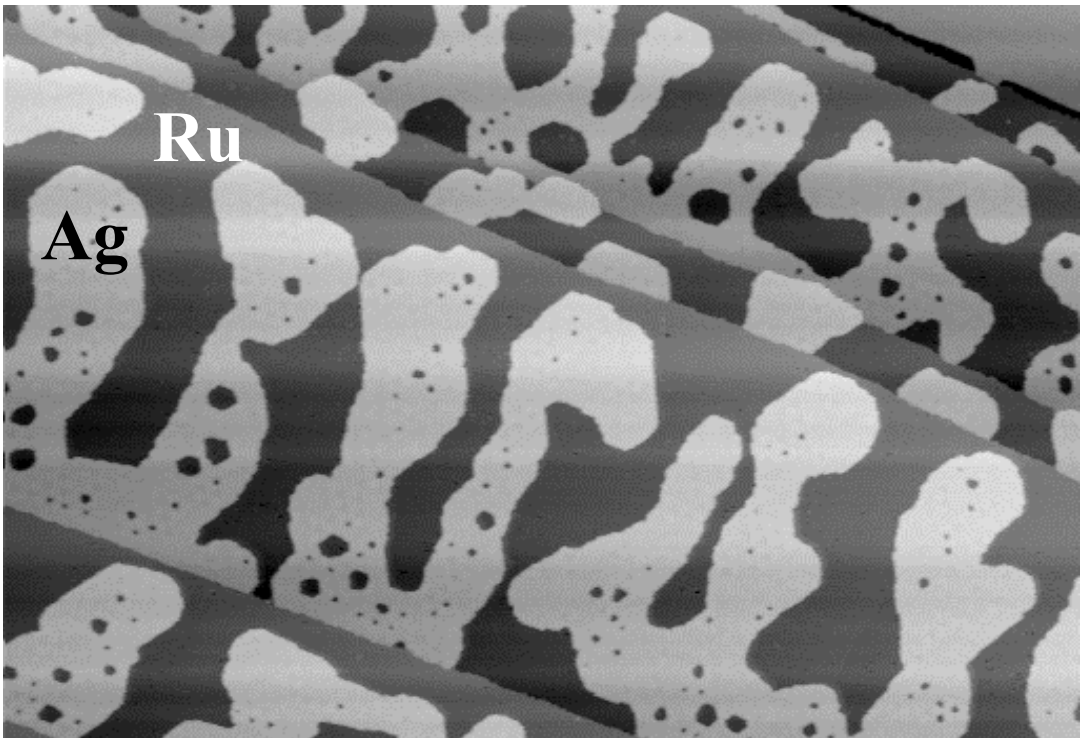

Figure 4. 220×300 nm^2 STM image of striped domains of Ag, oriented predominantly perpendicular to the Ru steps, and coexisting with vacancy islands. Here, $\theta_S \approx 0.4$ ML and $f \approx 0.5$.

Relation to the surface stress

Differences in surface stress, as we expect to find between Ag- and sulfur-covered Ru regions bounding an island step edge, are thought to cause the effective elastic interaction between vacancy islands[27]. In this framework, the strength of this elastic interaction is then simply given by $\gamma_d=(1-\nu)\sigma^2/(2\pi\varepsilon)$, where ν and ε are, respectively, the Poisson ratio and shear modulus of the substrate which mediates the interaction, and σ is the difference in the normal component of the surface stress between Ag and Ru regions. Assuming values for the Poisson ratio, $\nu_{Ru}\approx0.5$, and shear modulus, $\varepsilon_{Ru}\approx10^{10}$ N/m^2, of the Ru substrate, similar to those of other elemental metals, the estimate of γ_d above implies absolute values of $\sigma\approx0.3$-0.5 eV/Å^2. This is within the range reported for unreconstructed metal(111) surfaces[27], lending confidence in our central estimate of γ_d. We expect to narrow its uncertainty as more experimental data for this system are analyzed.

Finally, we comment on some disagreement in detail between the predictions of the elastic interaction model[25,26] and our experimental findings. Certainly, the model does not include effects of the island clustering (or density fluctuations) observed at low f (and possibly stabilized by an additional short-range attraction between islands). There is also disagreement on the expected and observed values of R and the average width of the stripes. Specifically, the model predicts a small increase in R with increasing f, but we measured a 30% decrease between f≈0.07 and 0.2. Also, theory predicts stripe widths almost an order of magnitude narrower than what we observed. We have not yet investigated the large f-regime, where a crystal of adatom islands is predicted to form[25,26], but expect additional complications. These differences are not surprising considering that the model overlooks many complexities specific to our system, from the processes involved in the reaction of the two metals with sulfur to the subsequent displacement of Ag.

In spite of these discrepancies of detail, there seems to be no doubt that strain-mediated interactions are truly effective ordering forces for the S/Ag/Ru(0001) crystal of vacancy islands. And that, although weak, they can be confidently measured, as we have shown here. Furthermore we have demonstrated the possibility of tuning the strain interactions to adjust the self-assembled patterns. This is shown in Figure 5 below. These ordering mechanisms are sufficiently general that the S/Ag/Ru(0001) crystal is unlikely to be unique: Small changes in the type of adsorbate or host film will probably produce new "quantum void" lattices with tunable parameters (R, b, λ, μ,...). An exciting possible application of vacancy lattices is as templates for pre-patterning new nano-structures[15], thus allowing properties which are unique to these length scales to be controlled. This relies on the detailed characterization, as done here, of the forces responsible for the existence of such templates.

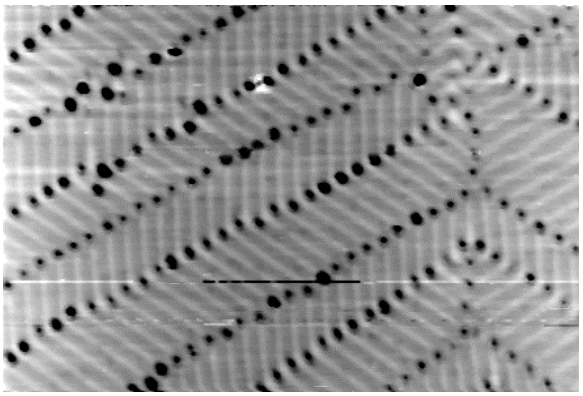

Figure 5. 200nm X 120nm image of a self-assembled nano-structure with chain structure.

We have tested the viability of using the S/Ag template structure in the case of deposition of Co onto the lattice. The result of one such deposition is shown in the STM image of Figure 6 below. The Co appears as darker gray portions, primarily situated around the edges of the remaining holes (see arrow in image). The presence of the Co has made the holes smaller, but have not completely filled them. The Co fills the holes from the edges, but cannot complete the hole because of the remaining sulfur.

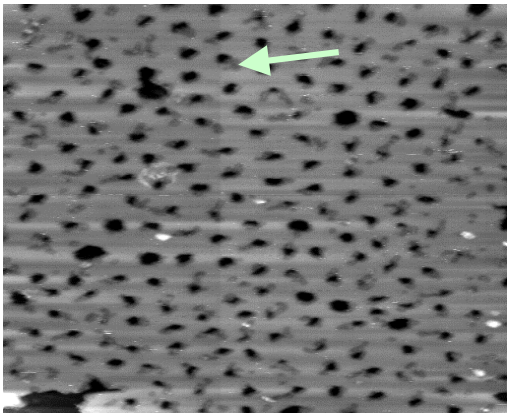

Figure 6. 600Å X 600Å STM image of a nano-template with the addition of Co. The Co is imaged as areas of slightly darker gray as compared to the Ag template as indicated by the arrow in the image

References

1. Seul, M. & Andelman, D. Domain shapes and patterns: the phenomenology of modulated phases. *Science* **267**, 476-483 (1995).
2. Schiffer, J. Sparse crystals. *Science* **279**, 675 (1998).
3. Evans, J.H. Observations of a regular void array in high purity Molybdenum irradiated with 2 MeV Nitrogen ions. *Nature* **229**, 403-404 (1971).
4. Asai, M., Ueba, H. & Tatsuyama, C. Heteroepitaxial growth of Ge films on the Si(100)-2×1 surface. *J. Appl. Phys.* **58**, 2577-2583 (1985).
5. Eaglesham, D.J. & Cerullo, M. Dislocation-free Stranski-Krastanow growth of Ge on Si(100). *Phys. Rev. Lett.* **64**, 1943-1946 (1990).
6. LeGoues, F.K., Copel, M. & Tromp, R.M. Microstructure and strain relief of Ge films grown layer by layer on Si(001). *Phys. Rev. B* **42**, 11690-11700 (1990).
7. Kern, K. *et al.* Long-range spatial self-organization in the adsorbate-induced restructuring of surfaces: Cu{110}-(2×1)O. *Phys. Rev. Lett.* **67**, 855-858 (1991).
8. Jäger, W. & Trinkaus, H. Defect ordering in metals under irradiation. *J. Nucl. Mater.* **205**, 394-410 (1993).
9. Hörnis, H., West, J.R., Conrad, E.H. & Ellialtioglu, R. Island ordering on clean Pd(110). *Phys. Rev. B* **47**, 13055-13058 (1993).
10. Zeppenfeld, P., Krzyzowski, M.A., Romainczyk, Ch., David, R. & Comsa, G. Stability of disk and stripe patterns of nanostructures at surfaces. *Surf. Sci.* **342**, L1131-L1136 (1995).
11. Haasen, P. *Physical metallurgy* (Cambridge Univ. Press, New York, 1996), p.256.
12. Alivisatos, A.P. Semiconductor clusters, nanocrystals, and quantum dots. *Science* **271**, 933-937 (1996).
13. Tersoff, J., Teichert, C. & Lagally, M.G. Self-organization in growth of quantum dot superlattices. *Phys. Rev. Lett.* **76**, 1675-1678 (1996).
14. Schuster, R., Röder, H., Bromann, K., Brune, H. & Kern, K. Stress relief via island formation of an isotropically strained bimetallic surface layer: the mesoscopic morphology of the Ag/Pt(111) surface alloy. *Phys. Rev. B* **54**, 13476-13479 (1996).
15. Parker, T.M., Wilson, L.K., Condon, N.G. & Leibsle, F.M. Epitaxy controlled by self-assembled nanometer-scale structures. *Phys. Rev. B* **56**, 6458-6461 (1997).
16. Grimes, C.C. & Adams, G. Evidence for a liquid-to-crystal phase transition in a classical, two-dimensional sheet of electrons. *Phys. Rev. Lett.* **42**, 795-798 (1979).
17. Fisher, D.S., Halperin, B.L. & Platzman, P.M. Phonon-ripplon coupling and the two-dimensional electron solid on a liquid-Helium surface. *Phys. Rev. Lett.* **42**, 798-801 (1979).
18. Hurd, A.J., Clark, N.A., Mockler, R.C. & O'Sullivan, W.J. Lattice dynamics of colloidal crystals. *Phys. Rev. A* **26**, 2869-2881 (1982).
19. J.L. Stevens, J.L. & Hwang, R.Q. Strain stabilized alloying of immiscible metals in thin films. *Phys. Rev. Lett.* **74**, 2078-2081 (1995).
20. Hwang, R.Q., Hamilton, J.C., Stevens, J.L. & Foiles, S.M. Near-surface buckling in strained metal overlayer systems. *Phys. Rev. Lett.* **75**, 4242-4245 (1995).
21. Morgenstern, K., Rosenfeld, G., Poelsema, B. & Comsa, G. Brownian motion of vacancy islands on Ag(111). *Phys. Rev. Lett.* **74**, 2058-2061 (1995).

22. de la Figuera, J., Prieto, J.E., Ocal, C. & Miranda, R. Creation and motion of vacancy islands on solid surfaces: a direct view. *Solid State Comm.* **89**, 815-818 (1994).
23. Our vacancy islands diffuse perhaps by atoms randomly moving around the islands edges, although other mechanisms involving a flow of step edge atoms across an island, or exchange of Ag edge atoms with the sulfur and Ag adatom gas, could be significant in this system.
24. Each hop averages 50 Å, between positions seemingly related to the original network of dislocations. From the hop rate, and the observed dissociation rate of several clusters of islands, we estimate single-bond energies of 0.26 eV between nearest-neighbor island pairs, but larger than 0.30-0.35 eV for multiply-bonded configurations (assuming Arrhenius-type rates).
25. Vanderbilt D. Phase segregation and work-function variations on metal surfaces: spontaneous formation of periodic domain structures. *Surf. Sci.* **268**, L300-L304 (1992).
26. Ng, K.-O. & Vanderbilt D. Stability of periodic domain structures in a two-dimensional dipolar model. *Phys. Rev. B* **52**, 2177-2183 (1995).
27. Ibach, H. The role of surface stress in reconstruction, epitaxial growth and stabilization of mesoscopic structures. *Surf. Sci. Rep.* **29**, 193-263 (1997).
28. Nelson, D.R & Halperin, B.I. Dislocation-mediated melting in two dimensions. *Phys. Rev. B* **19**, 2457-2484 (1979).
29. Huse, D.A. Shape of diffraction peaks of a two-dimensional solid. *Phys. Rev. B* **28**, 6110-6111 (1983).
30. The form of the elastic Hamiltonian assumes that the Ru surface deforms in reaction to the elastic relaxations near the step edges[25,26]. That strain in the Ag film can deform the Ru substrate is consistent with the results in ref 20.
31. Morgenstern, K., Rosenfeld, G. & Comsa, G. Decay of two-dimensionl Ag islands on Ag(111). *Phys. Rev. Lett.* **76**, 2113-2116 (1996).

This page intentionally left blank

II. EVAPORATION-INDUCED SELF-ASSEMBLY (EISA)

Mesoporous silica thin films prepared by self-assembly may provide a viable strategy for selective area growth of nanoarrays with feature dimensions that are unattainable using conventional lithographic techniques. These films may be used as a means to grow semiconductor crystals from the substrate surface by CVD; the crystals would grow through the pores and then grow laterally on the surface of the mesoporous silica. Ultimately, this process may allow epitaxial growth on surfaces with large lattice mismatches. Important considerations are the presence of line-of-sight porosity and thermal stability of the EISA film as well as the degree to which the film 'transparency' can be altered via manipulation of the pore aspect ratio (width vs depth) and the film mesophase (cubic vs. hexagonal). This section describes the process of evaporation-induced-self-assembly (EISA) of sol-gel based mesoporous silica films and provides several examples of films that were evaluated as candidates to enhance selective area deposition.

Self-Assembly

A general definition of self-assembly is the spontaneous organization of materials through noncovalent interactions (hydrogen bonding, Van der Waals forces, electrostatic forces, π−π interactions, etc.) with no external intervention. Self-assembly typically employs asymmetric molecules that are pre-programmed to organize into well-defined supramolecular assemblies. Most common are amphiphilic surfactant molecules or polymers composed of hydrophobic and hydrophilic parts. In aqueous solution above the critical micelle concentration (cmc), surfactants assemble into micelles, spherical or cylindrical structures that maintain the hydrophilic parts of the surfactant in contact with water while shielding the hydrophobic parts within the micellar interior (see Figure 1). Further increases in surfactant concentration result in the self-organization of micelles into periodic hexagonal, cubic, or lamellar mesophases (Figure 1).

Obviously such detergent mesophases do not themselves represent robust engineering materials suitable for nanotechnologies. However in 1992 Mobil researchers[1] discovered that surfactant self-assembly conducted in aqueous solutions of soluble silica species results in spontaneous co-assembly of silica-surfactant mesophases. Surfactant removal creates periodic mesoporous solids, essentially silica fossils of the liquid-crystalline assembly. Over the last eight years, this pioneering work has been extended to produce a wide compositional range of mesoporous solids, and, using a variety of surfactants, the pore sizes have been varied in the approximate range, 1 nm to over 10 nm[2-6]. Despite excellent control of pore size, early mesoporous materials were made in the form of powders, precluding their use in thin film applications like membranes, low dielectric constant interlayers, and optical sensors. Stable, supported, mesoporous silica films were reported in 1996[7-9]. Typically, substrates were introduced into silica/surfactant/solvent systems used to prepare bulk hexagonal mesophases (initial surfactant concentrations c_o > cmc). Under these conditions, hexagonal silica-surfactant mesophases are nucleated on the substrate with pores oriented parallel to the substrate surface. Growth and coalescence over a period of hours to weeks resulted in continuous but macroscopically inhomogeneous films characterized by granular textures on micrometer-length scales.

Evaporation-Induced Self-Assembly (EISA)

Consideration of Figure 1 in the context of sol-gel dip-coating suggests an alternative route to the formation of thin film mesophases. Beginning with a homogeneous solution of soluble silica and surfactant prepared in ethanol/water solvent with c_o << cmc, preferential evaporation of ethanol concentrates the depositing film in water and nonvolatile surfactant and silica species (Figure 2). The progressively increasing surfactant concentration drives self-assembly of silica-surfactant micelles and their further organization into liquid-crystalline mesophases[10-12]. Pre-existing, incipient silica-surfactant mesostructures (which exist at solid-liquid and liquid-vapor interfaces at c < cmc) serve to nucleate and orient mesophase development[7,13]. The result is rapid formation of thin film mesophases that are highly oriented with respect to the substrate surface. Through variation of the initial alcohol/water/surfactant mole ratio it is possible to follow different trajectories in composition space (see Figure 2b) and to arrive at different final mesostructures. For example, using cetyltrimethylammonium bromide (CTAB), we demonstrated the formation of 1-D hexagonal, cubic, 3-D hexagonal and lamellar silica-surfactant mesophases[9-11]. Transmission electron micrographs of representative cubic thin film mesophases are shown in Figure 3. Such cubic mesophases are crucial for applications that require guaranteed pore accessibility and through-film pore connectivity.

The dip-coating scheme depicted in Figure 2 represents a rapid (~10s), dynamic self-assembly process conducted in a rather steep concentration gradient. Its steady, continuous nature promotes continuous accretion of micellar or perhaps liquid-crystalline species onto interfacially organized mesostructures. Large, liquid-crystalline domains grow progressively inward from the solid-liquid and liquid-vapor interfaces (with increasing distance above the reservoir surface, Figure 2). Deposited films are optically transparent and completely featureless on the micrometer-length scale.

Essential to our ability to rapidly organize thin film mesophases is suppression of inorganic polymerization under acidic conditions at a hydronium ion concentration corresponding closely to the isoelectric point of colloidal silica ($[H_3O^+]$) ~0.01)[14]. By first turning off siloxane condensation, we allow cooperative silica-surfactant self-assembly to proceed unimpeded, and the resulting as-deposited films exhibit liquid-crystalline (semi-solid) behavior. Subsequent aging, exposure to acid or base catalysts, or thermal treatment can solidify the silica skeleton, thereby locking in the desired mesostructure.

Evidence for the liquid-crystalline nature of as-deposited films is several-fold: First, using a cantilever beam technique we showed there to be dramatically less tensile stress developed during mesophase thin film deposition (5-10 MPa) compared to deposition of the same silica sol prepared without surfactants (~200 MPa). This virtual absence of drying stress suggests that the films completely dries prior to solidification (i.e., as-deposited films are not solidified). Second, we have shown that as-deposited mesophase films can be transformed to completely different mesophases (e.g., lamellar → cubic)[10]. Third, the as-deposited films exhibit self-healing tendencies. These combined liquid-crystalline characteristics make the EISA process robust yet versatile and provide of thermal stability and tailored porosity, e.g. line-of-sight porosity, pore uniformity, pore accessibility and through-film pore connectivity.

Examples of Sol-Gel Derived Thin Films for Selective Area Growth (SAG)

We studied the influence of various amphiphilic structure directing agents (surfactants, di- and triblock copolymers) on the size, orientation, and connectivity of pores of the corresponding thin film mesophases prepared by evaporation-induced self-assembly. Examples of these films are discussed in this section.

Angle-resolved XPS line-of-sight porosity measurements and optimization of pore aspect ratios in self-assembled films. SiO_2 films (prepared as in Figure 3) via sol-gel processes (aerosol deposition) on sapphire and Si(100) substrates were characterized with XPS as a function of both azimuthal detection angle and temperature and with SEM. The results suggest strongly that aerosol-deposited films may not be well suited for selective area growth (SAG) templating. Although the films appear featureless in initial micrographs, subsequent XPS and SEM evaluation are consistent with the presence of areas of non-uniformity (on the order of microns over ¼-½ of the surface) due to poor wetting. Based on previous experience in systematic SAG kinetics measurements, we believe exposed substrate areas on this scale will likely dominate nucleation and growth during subsequent CVD nitride deposition. The resulting depletion of precursors in the gas-phase is expected to leave the high aspect ration self-assemble nanopores unable to compete effectively for nitride deposition. The thermal stability of a Brij-56 film (see Figure 3) was studied by XPS and found to be stable to at least 1300 K.

Pore studies using block co-polymers. Due to their relatively low molecular weight, the surfactant templated films discussed above have been limited to mesoscopic order and relatively small characteristic length scales. In order to increase the 'transparency' of the films to CVD infiltration explored the use of polystyrene-polyethylene oxide diblock (PS-PEO) and triblock copolymers (PEO-PS-PEO), both of which are commercially available and water- and alcohol-soluble, as a means to increase the pore size from about 2.5-nanometers (obtained for surfactant templated films in Figure 3) to approximately 20 nanometers[19,20]. Conceivably, both the meso-scale pore size and macroscale feature sizes could influence subsequent CVD infiltration. The synthesis process began with a dilute homogeneous solution of a silica precursor and the copolymer in a mixture of tetrahydrofuran (THF, a good solvent for both PS and PEO) and water. Following casting of the solution of a surface, the THF preferentially evaporated resulting in concentration of the film components and simultaneous self-assembly of both the PS-PEO polymers and the silicate. Consequently, liquid-crystalline mesophases were generated and mesoporous silica films were achieved upon copolymer removal. Figure 4 shows the TEM image of a diblock film and demonstrates the porous ordered nanostructure and pore diameter approaching 20 nm**.**

Ultrathin nanoporous silica. We also continued to explore the aerosol assisted self-assembly process as a means to make highly uniform, extremely thin films – again to enhance transparency. Figure 5 shows an ultrathin (approximately 50nm-thick) film prepared using Brij56 as the pore-directing agent.

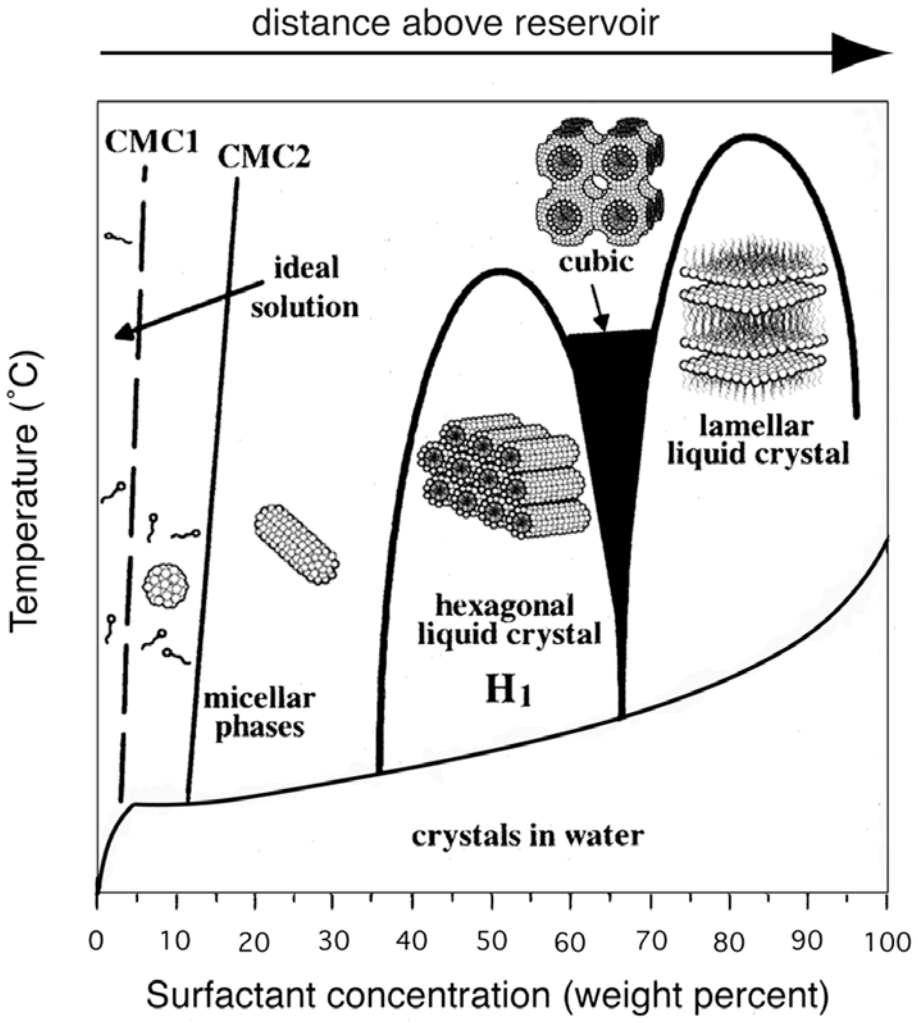

Figure 1. Schematic phase diagram for CTAB in water. Arrow denotes evaporation-driven pathway during dip-coating, aerosol processing, etc. Adapted from Raman et al.[15]

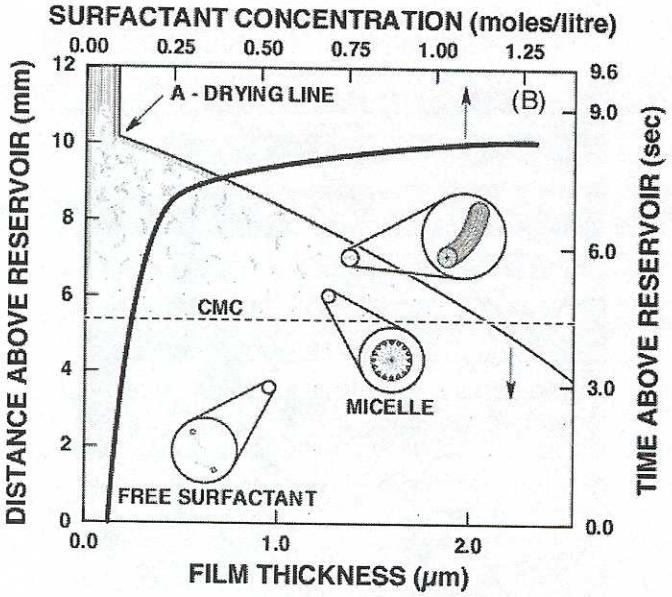

Figure 2 (a)

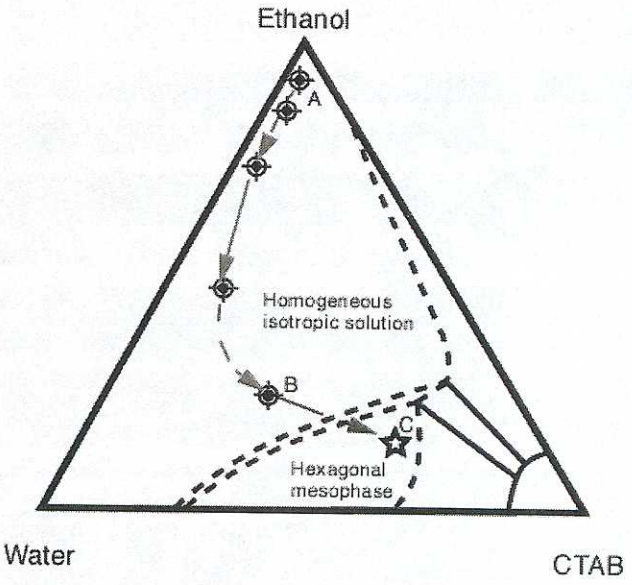

Figure 2 (b)

Figure 2. **(a)** Steady-state film thinning profile established during dip-coating of a complex fluid comprising soluble silica, surfactant, alcohol, and water. Initial surfactant concentration c_o << cmc. Surfactant concentration increases with distance above the reservoir surface. **(b)** Approximate trajectory taken in ethanol/water/CTAB phase space during dip-coating. Point A corresponds to the initial composition of entrained solution. Point B is near the drying line, and Point C corresponds to the dried film. Pathway calculated by combining results of in situ probe experiments[16] and imaging ellipsometry[17], and superimposing data onto the experimental phase diagram determined by Fontell et. al.[18].

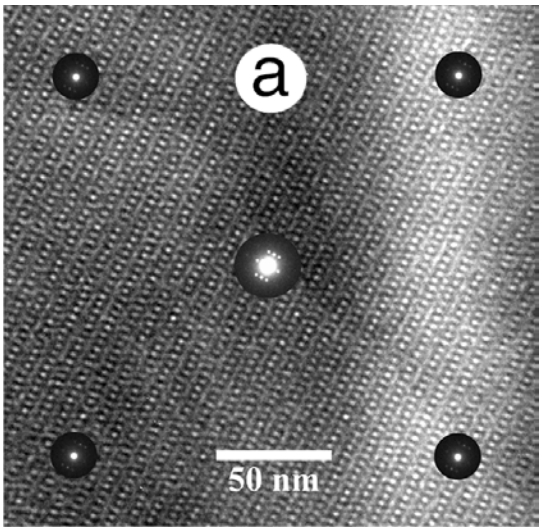

Figure 3 (a)

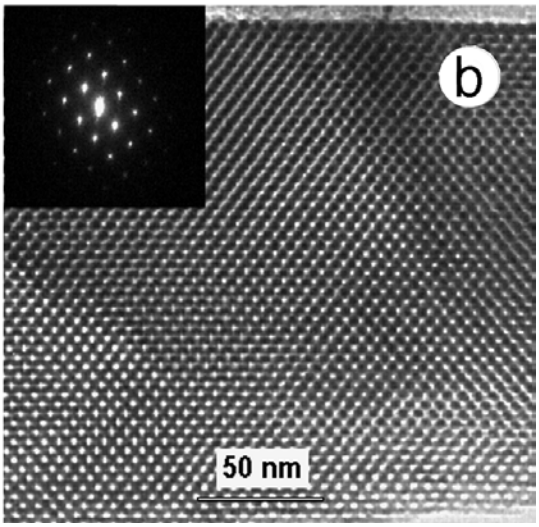

Figure 3 (b)

Figure 3. Representative TEM micrographs of cubic thin film mesophases prepared by aerosol processing. **(a)** TEM plan view of calcined film prepared from CTAB, showing large [210]-oriented domain of cubic mesophase, pore diameter is about 2.5 nm. **(b)** Cross-sectional TEM of calcined cubic film formed from the nonionic surfactant, Brij-56.

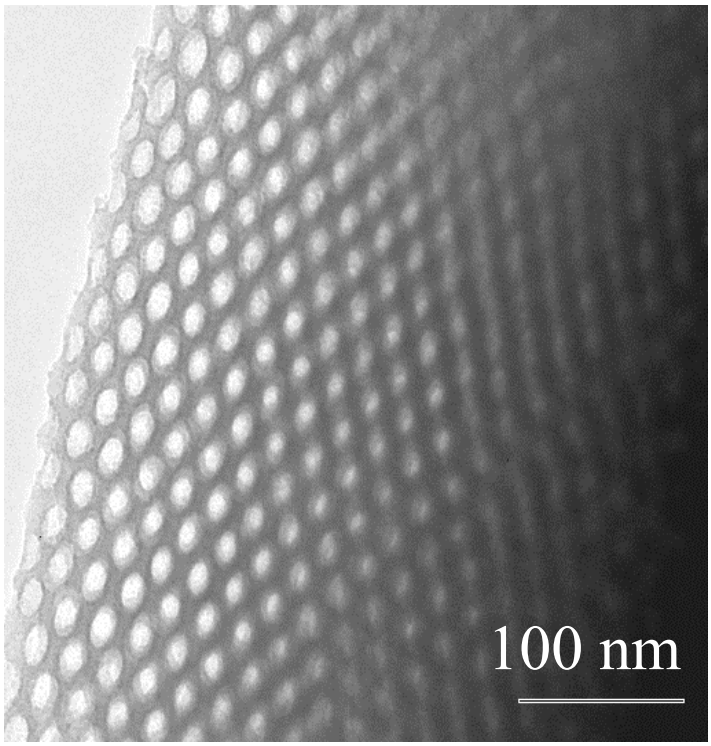

Figure 4

Figure 4. TEM micrograph of cast-film prepared PS(215)-PEO(100) diblock in silica (2 wt% solution of polymers in THF). Pore size of approximately 18 nm was achieved following removal of polymer phase by calcination at 450°C for three hours.

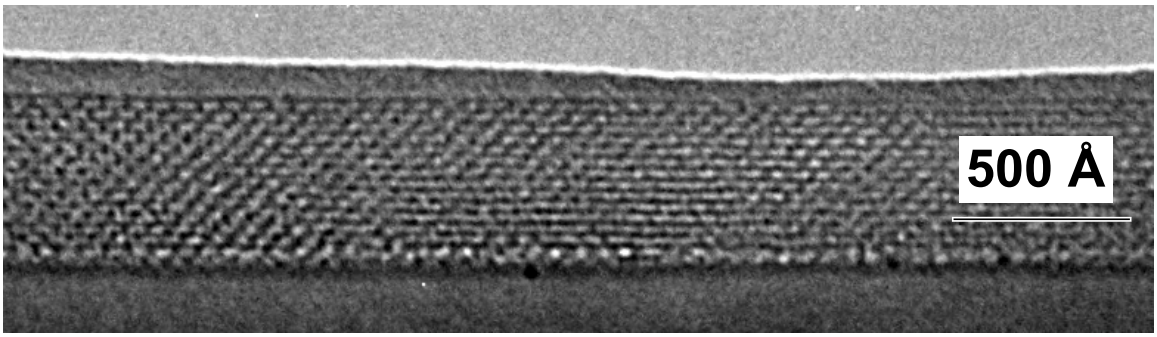

Figure 5

Figure. 5. TEM micrograph of an ultrathin nanoporous silica film templated using Brij56, $(CH_3(CH_2)_{15}(OCH_2CH_2)_{10}OH)$.

References

1. C. Kresge, M. Leonowicz, W. Roth, C. Vartuli, J. Beck, *Nature* 1992, **359**, p. 710
2. Q. Huo, D. Margolese, U. Ciesla, P. Feng, T.G. Gier, P. Sieger, R. Leon, P.M. Petroff, F. Schuth, G. Stucky, *Nature* 1994, **368**, p. 317
3. A. Firouzi, D. Kumar, L.M. Bull, T. Besier, P. Sieger, Q. Huo, S.A. Walker, J.A. Zasadzinski, C. Glinka, J. Nicol, D. Margolese, G.D. Stucky, B.F. Chmelka, *Science* 1995, **267**, p. 1138
4. P.T. Tanev, T.J. Pinnavaia, *Science* 1995, **267**, p. 865
5. D.M. Antonelli, J.Y. Ying, *Angew. Chem. Int. Ed. Engl*. 1995, **34**, p. 2014
6. D. Zhao, J. Feng, Q. Huo, N. Nelosh, G. Fredrickson, B. Chmelka, G.D. Stucky, *Science* 1998, **279**, p. 548
7. I. Aksay, M. Trau, S. Manne, I. Honma, N. Yao, L. Zhou, P. Fenter, P. Eisenberger, S. Gruner, *Science* 1996, **273**, p. 892
8. H. Yang, A. Kuperman, N. Coombs, S. Mamiche-Afara, G.A. Ozin, *Nature* 1996, **379**, p. 703
9. M. Ogawa, *Chem. Commun*. 1996, p. 1149
10. Y. Lu, R. Ganguli, C. Drewien, M. Anderson, C. Brinker, W. Gong, Y. Guo, H. Soyez, B. Dunn, M. Huang, J. Zink, *Nature* 1997, **389**, p. 364
11. P.J. Bruinsma, A.Y. Kim, J. Liu, S. Baskaran, Chem. Mater. 1997, **9**, p. 2507
12. M. Ogawa, *J. Am. Chem. Soc*. 1994, **116**, p. 7941
13. H. Yang, N. Coombs, I. Sokolov, G.A. Ozin, *Nature* 1996, **381**, p. 589.
14. C. J. Brinker, G.W. Scherer, *Sol-Gel Science*, Academic Press, 1990.
15. N. Raman, M. Anderson, C. Brinker, *Chem. Mater*., 1996, **8**, p. 1682.
16. F. Nishida, J. McKiernan, B. Dunn, J. Zink, C. Brinker, A. Hurd, *J. Am. Ceram. Soc*. 1995, **78**, p. 1640
17. R. Ganguli, *Mesoporous Thin Silica Films Created by the Templating of CTAB Mesophases*, Masters Thesis, Chemical & Nuclear Engineering, University of New Mexico, Albuquerque, NM.
18. K. Fontell, A. Khan, B. Lindstrom, D. Maciejewska, S. Puang-Ngern, *Colloid Poly. Sci*. 1991, **269**, p. 727.
19. K. Yu, C.J. Brinker, A.J. Hurd, A. Eisenberg, "Synthesis of Silica/Polystyrene-block-Poly(ethylene oxide) Films with Regular and Reverse Mesostructures of Large Characteristic Length Scales by Solvent Evaporation-Induced Self-Assembly", manuscript in preparation.
20. K. Yu, A. Frischknecht, C. Drewien, A.H. Hurd, C.J. Brinker, J.G. Curro, A. Eisenberg, "Formation Mechanism of Silica/Diblock Mesophases by Solvent Evaporation-Induced Self-Assembly", manuscript in preparation.

III. KINETICS AND TRANSPORT IN GALLIUM NITRIDE EPITAXIAL LATERAL OVERGROWTH AND ITS APPLICATION TO SOL-GEL BASED SIO2 FILMS

Michael E. Bartram, Christine C. Mitchell, and Michael E. Coltrin
Sandia National Laboratories
Albuquerque, NM 87185-0601

We have investigated lateral transport mechanisms in Epitaxial Lateral Overgrowth (ELO) of GaN grown by Metal Organic Chemical Vapor Deposition. ELO growth rate profiles on exposed line patterns were examined with and without the presence of deep trenches in the surrounding dielectric mask. The growth profiles remained unchanged in the two sets of experiments, showing that gas-phase diffusion, rather than diffusion on the surface of the mask, is the dominant lateral mass-transport mechanism. A systematic experimental and theoretical study of ELO growth efficiency is reported. When the heterogeneous growth chemistry is very fast, ELO efficiency is essentially 100%, and the system is transport limited. As the chemistry rate drops, due to lower temperature for example, efficiency is shown to drop.

INTRODUCTION

Epitaxial Lateral Overgrowth (ELO), a variation of selective area growth, is now widely used to improve the material quality in the growth of high quality GaN thin films (1-7). In this technique, a GaN buffer layer is grown on sapphire, SiC, or Si, followed by deposition of a blanket layer of dielectric material. The dielectric is photolithographically patterned and then etched, exposing portions of the underlying GaN buffer layer. Continued GaN re-growth proceeds selectively only upon the exposed GaN regions. It is found that the defect density of the laterally overgrown material can be two orders of magnitude smaller than for the normal, unpatterned GaN growth.

This technique is normally performed on patterns with dimensions in the micron regime. It can however be theoretically transferred to patterns with dimensions in the nano-regime. One possible technique for fabricating masks with growth zones that are 5-10 nm wide is by depositing SiO_2 films via sol-gel processes on sapphire and other substrates. If these films can be deposited in a uniform film with evenly spaced regions of masked and non-masked material the ELO growth should proceed in the same manner as larger dimension patterns.

Initial samples of sol-gel SiO_2 films on sapphire substrates did not produce films that had a uniform distribution of nucleation zones. Preliminary results via scanning electron microscope (SEM) indicated non-uniform wetting leaving zones without SiO_2 that ranged from 0.25 – 0.5 microns. The thermal stability of these films was analyzed with XPS. In lieu of sol-gel based SiO_2 films we continued to study the kinetics of selective area GaN growth with micron sized patterns. Specifically patterns were used that would demonstrate the growth progression from both concave and convex corners. This would be relevant when trying to grow from patterns other than straight parallel lines. This would be the case for SiO_2 films applied via a sol-gel mechanism.

RESULTS OF SOL-GEL FILM STUDIES VIA SEM AND XPS

SiO2 films deposited via sol-gel processes on sapphire and Si(100) substrates were characterized with XPS as a function of both azimuthal detection angle and temperature and with SEM. The results suggest strongly that these films are not well-suited for selective area growth (SAG) templating as envisioned in our proposal originally. Although contrary to previous SEM measurements in which the film surfaces were thought to be featureless, our XPS and SEM measurements are consistent with the presence of large openings in the thin films (non-uniform wetting) having dimensions on the order of microns over 1/4 to 1/2 of the surface. Based on previous experience in systematic SAG kinetics measurements, we believe exposed substrate areas of this magnitude will likely dominate nucleation and growth during nitride deposition. The resulting depletion of precursors in the gas-phase is expected to leave the high aspect ratio self-assembled nano-pores unable to compete effectively for nitride deposition. Although these results imply that using sol-gel films for SAG strategies in CVD nitrides may not be a promising focus, for the sake of completeness the thermal stability of one of these sol-gel films was studied with XPS. Sol-gel film B56 on sapphire was shown to be stable (maintain the same photoelectron "transparency" characteristics) to at least 1300K.

Table 1.
FILMS/SUBSTRATES EXAMINED:

	B56 (~2.5nm pore/2.5nm wall)	P123 (~10nm pore/3nm wall)
Sapphire:	x	x
Si(100):	x	x
Ave. dens.:	0.80	0.53 (WRT non-porous SiO2)

Table 2.

ANNEALING TEMPERATURES FOR SOL-GEL FILM B56 ON SAPPHIRE:

phi \ T	300K	800K	1000K	1300K
0 deg.	x	x	x	x
25	x	x	-	-
45	x	x	-	-
65	x	x	x	x

(phi=photoelectron detection angle with respect to the surface normal.)

REFERENCE INFO.

Film thicknesses expected:	~40nm(based on previous TEM measurements)
Al Kalpha X-ray energy:	1,486.6 eV
Binding energy for Si2p, Al2p:	~ 100 eV, ~ 75 eV
Photoelectron kinetic energy:	~ 1,400 eV
Mean free escape depth @ 1400eV:	lambda ~ (KE^0.75)/10 ~ 2.3 nm
Photoelectron signal~0:	4 lambda ~ 9 nm
Survey scans:	1400 – 0 eV, film composition plus carbon only
phi:	photoelectron detection angle WRT the surface normal.

Although 1400eV photoelectrons should be attenuated fully by a film thicker than 9nm, these should be detectable through 40nm of SiO2, given pores with a line-of-sight to the substrate. If the pores are aligned in the direction of the surface normal, then the signal would be expected to decrease as phi is increased. When phi is increased such that ~3 walls of the pores are penetrated (~3-4 lambda) the photoelectron signal would be expected to go to zero. For the B56 sol-gel films this means that this "critical" phi should be ~20deg. For the P123 films, phi-critical should be ~45deg. However, such a signal decrease was not observed in our study. In fact, under no circumstance were signals from the substrates attenuated fully at angles up to 65deg (the maximum phi attempted). Neither were differences observed for ANY film on ANY substrate as a function of phi. The fall-off in substrate signal strength as a function of angle in all cases reached minima of only ~33% at 65deg (normalized to the thin film reference Si2p peak [SiO2]).

Alternatively, an upper limit on the "effective" film thickness can be estimated by (1) calculating the average densities for the sol-gel films (given in Table 1. based on pore sizes measured with TEM) and (2) assuming the minimum signal observed with XPS at 65deg. is representative of signal that is "almost" fully attenuated. In this case:

The effective film thickness = 4 lambda cos phi / Ave.dens.

This yields an effective thickness (or average thickness) of 4.8 and 7.6 nm for sol-gels B56 and P123, respectively. Obviously, these extremes are unreasonable for uniform film thickness, especially in view of previous TEM measurements (see Reference Info above). These estimates of the average thickness suggest these films must be non-uniform or in other words the surface is "wetted" non-uniformly. Based on this, we expect the films could well be on the order of 40 nm thickness but - with large openings where the substrate remains uncovered by SiO2. Such openings would allow photoelectron signals to be observed at large values of phi.

Although these results imply that using sol-gel films for SAG strategies in CVD nitrides may not be a promising focus, for the sake of completeness, the thermal stability of one of these sol-gel films was studied with XPS. For sol-gel film B56 on sapphire, the same photoelectron "transparency" characteristics as a function of detection angle were maintained at the highest temperature accessible with our apparatus of 1300K. This suggests sol-gel SiO2 films on sapphire may be thermally stable at CVD nitride temperatures, at least with respect to features on the scale of microns.

Previous SEM measurements have described the films on Si(100) as being featureless. Our SEM experiments are not consistent with this. On all substrates, SEM shows features consistent with the presence of large openings in the thin films (non-uniform wetting) having dimensions on the order of microns over 1/4 to 1/2 of the surface. Unfortunately, EDX lacks sufficient lateral resolution for the elements in question to verify the features are in fact areas of exposed substrate. However, the XPS results are most reasonably consistent with this suggestion.

GROWTH KINETICS FROM CONCAVE AND CONVEX SIO2 PATTERNS

ELO growth is a method where SiO_2 or another dielectric is patterned on top of a base layer of GaN to open up nucleation zones in the mask from which a subsequent growth of GaN proceeds. GaN is a hexagonal growth system therefore the relevant orientations with respect to the underlying GaN will be 30 degrees apart. The mask patterns can be oriented in two different primary directions with vastly different growth results. If the pattern edge runs along the $[1\bar{1}00]$ direction the resulting overgrowth will produce a $(11\bar{2}2)$ face. We will call this the fast growth direction and refer to the face as the fast face. The alternate orientation is when the pattern edge runs along the $[11\bar{2}0]$ direction. This case, which we will call the slow growth direction, produces features with $(1\bar{1}01)$ faces. We will refer to these faces as slow growing faces. This terminology for fast and slow growing faces refers to the rate at which the faces laterally overgrow the mask and is indicative of the growth kinetics.

The most common way to pattern a wafer is to arrange a series of long parallel lines spaced some distance apart so that growth proceeds laterally over the mask away from the nucleation zone and will coalesce with an adjacent stripe. Using this method you can grow a

coalesced film of laterally overgrown GaN. To study the behavior of this growth more detailed mask patterns will have to be used. Instead of just straight long parallel lines the fast and slow growing faces can be arranged so that the growth will proceed from either a convex or concave corner. To determine whether a corner is convex or concave first look at the direction the GaN will be growing over the mask. A convex corner is present when the angle between the two sides, measured away from the nucleation zone, is greater than 180 degrees. A concave corner is present when the angle, again measured away from the nucleation zone, is less than 180 degrees. We will call growth from convex corners outward growth and growth from concave corners inward growth. Figure 1 shows a hexagonal nucleation zone where both outward and inward growth occurs. In this figure, the black solid lines in a hexagon shape show the original nucleation zone. This pattern has six convex corners defined by adjacent fast faces. 240° separate the defining edges of the nucleation zone. This pattern also has six concave corners. They are the corners that are separated by 120°.

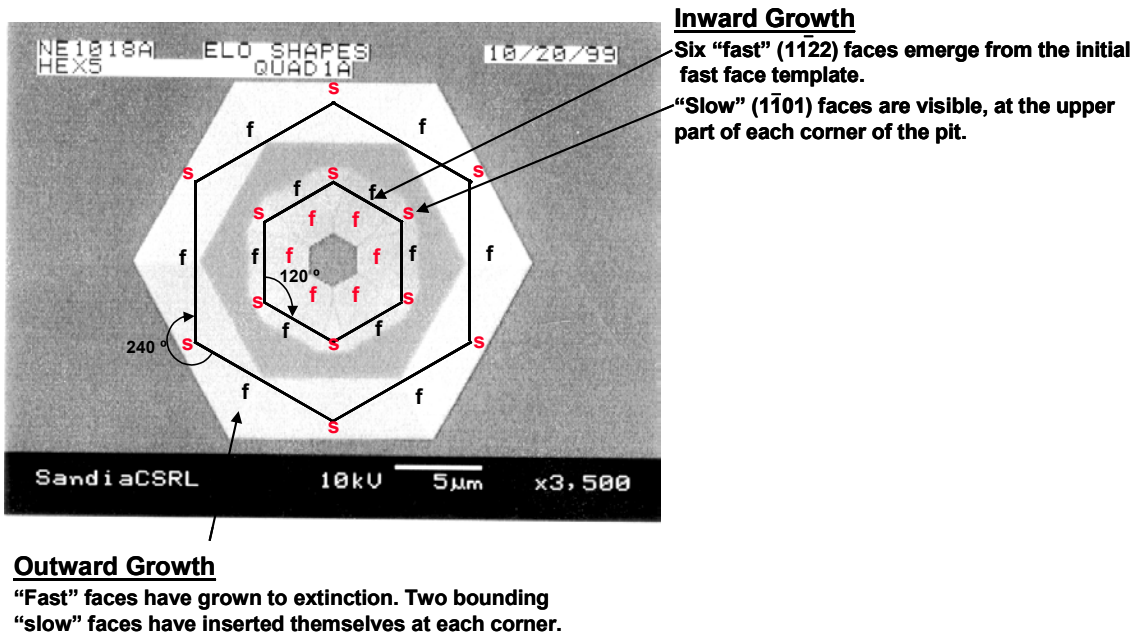

Figure 1. A SEM picture with GaN growth from a hexagon nucleation zone, shown by overlaid black lines, demonstrates "outward" and "inward" growth.

Figure 1 shows convex corners that are defined by edges running in the $[1\bar{1}00]$ "fast" direction. If these edges were infinitely long or the time was very short $(11\bar{2}2)$ faces would be present. Because the $(11\bar{2}2)$ face grows faster than the $(1\bar{1}01)$ face the six $(11\bar{2}2)$ faces have

grown to extinction leaving all slow faces showing on the outside of the feature. Growth runs stopped earlier in time, show that there is a time period where the fast faces and slow faces exist concurrently. As time progresses the surface area of the fast faces is reduced while the surface area of the slow faces increases. Figure 2 If the pattern had been arranged so that the GaN was growing from six edges orientated in the slow direction, the fast faces would never have a presence. The resulting feature would be the same as shown in Figure 1.

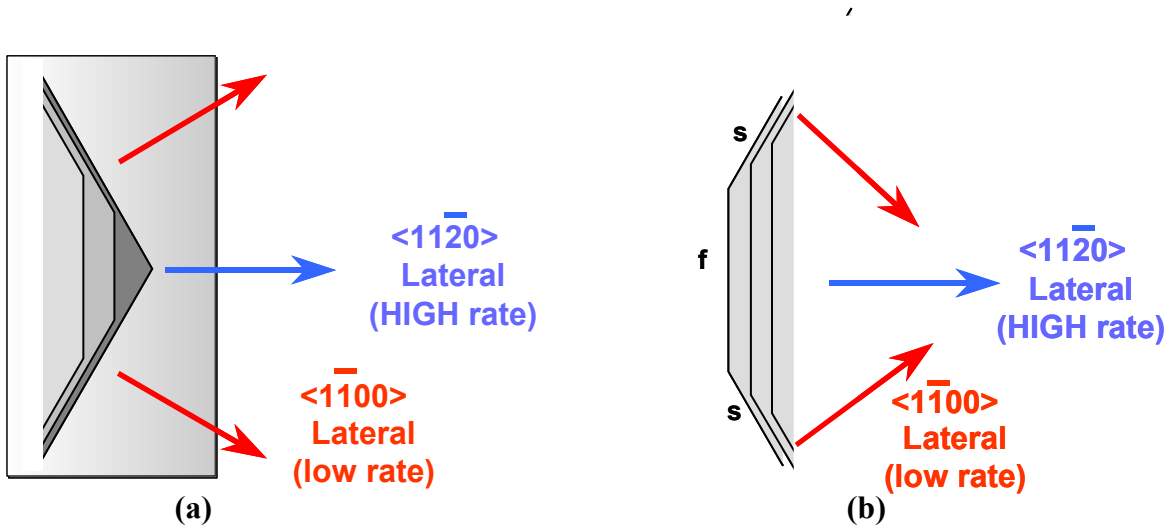

Figure 2. **(a)** Illustration of growth from convex corners "outward growth" shows graphically how the fast growing face is overcome by the slower growing face. **(b)** Illustration of growth from concave corners "inward growth" shows graphically how the slow growing face is dominated by the fast growing face.

Growth from concave corners presents us with a different situation. If the growth starts from a pattern orientated in the fast growth direction we find that after a substantial amount of time, fast faces dominate the inward growth. This could be simply explained by the fact that the growth started from a fast template and was thereby influenced into this growth mode. However, when we start from a pattern configured using slow faces we also find that the fast faces dominate the inward growth. Figure 2 illustrates this result in with a geometrical argument. As the fast and slow faces grow for the same period of time the fast face makes more lateral progress than the slow face does. As this occurs the fast face eventually dominates the slow face. The result is that independent of the orientation of the pattern growth from concave corners is dominated by the fastest laterally growing face.

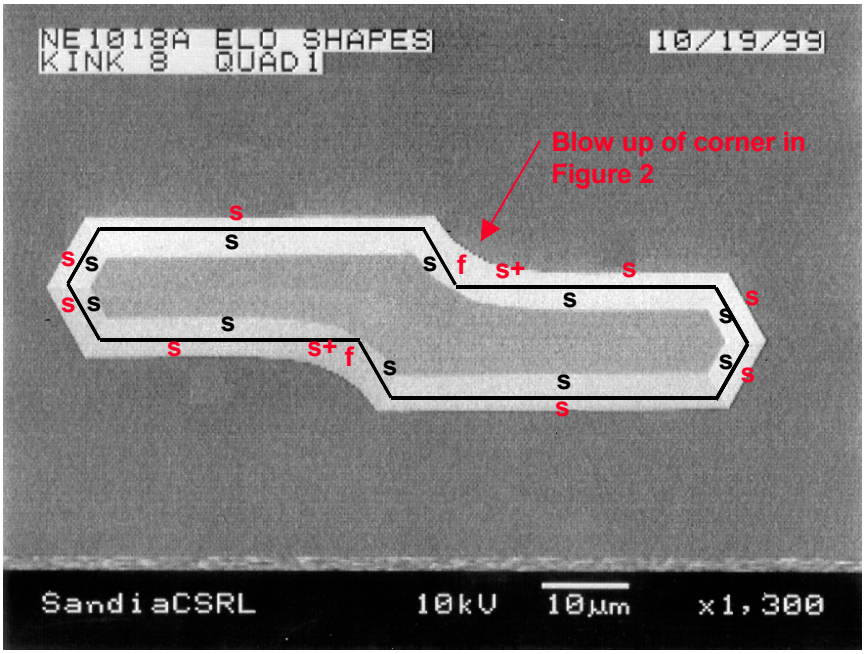

Figure 3. SEM picture of GaN growth from a nucleation zone with both concave and convex corners. This demonstrates insertion of multiple faces from concave corners.

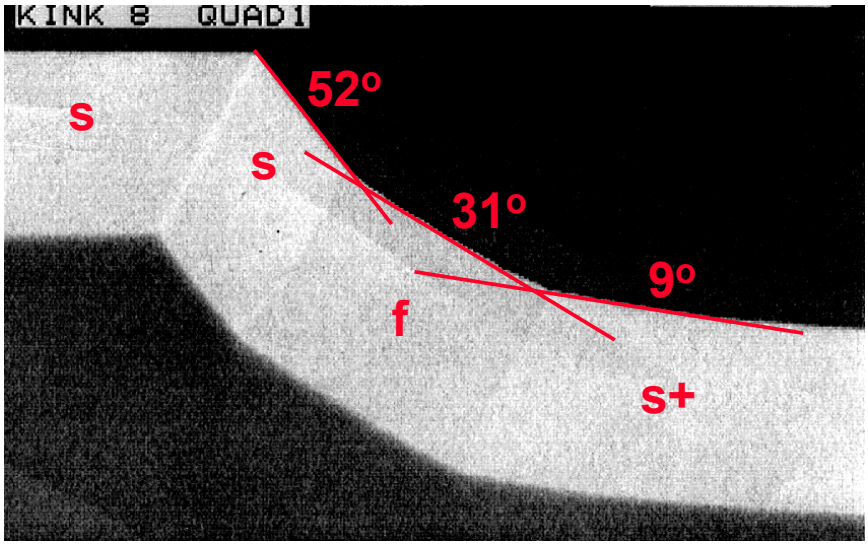

Figure 4. High magnification SEM of concave corner in Figure 3 shows the insertion of multiple faces.

ACKNOWLEDGMENTS

This work was supported by DOE Office of Basic Energy Sciences. Sandia is a multiprogram laboratory operated by Sandia Corporation, a Lockheed Martin Company, for the United States Department of Energy under Contract DE-AC04-94AL85000. We wish to thank R. G. Shul and C. G. Willison for etching the Si wafers used in these experiments, J. J. Figiel and K. Waldrip for technical assistance in the MOCVD growth, G. Lopez for technical support in wafer patterning, and M. E. Bartram, who designed the ELO mask used in the growth efficiency studies.

REFERENCES

1. Y. Kato, S. Kitamura, K. Hiramatsu, and N. Sawaki, *J. Cryst. Growth*, **144,** 133 (1994).
2. S. Kitamura, K. Hiramatsu, and N. Sawaki, *Jpn. J. Appl. Phys.*, **34,** L1184 (1995).
3. T. Tanaka, K. Uchida, A. Watanabe, and S. Minagawa, *Appl. Phys. Lett.*, **68,** 976 (1996).
4. K. Hiramatsu, S. Kitamura, and N. Sawaki, *Mat. Res. Soc. Symp. Proc.* , **395,** 267 (1996).
5. X. Li, A. M. Jones, S. D. Roh, D. A. Turnbull, S. G. Bishop, and J. J. Coleman, *J. Electron. Mater.*, **26,** 306 (1997).
6. O.-H. Nam, M. D. Bremser, T. S. Zheleva, and R. F. Davis, *Appl. Phys. Lett.*, **71,** 2638 (1997).
7. D. Kapolnek, S. Keller, R. Vetury, R. D. Underwood, P. Kozodoy, S. P. DenBaars, and U. K. Mishra, *Appl. Phys. Lett.*, **71,** 1204 (1997).
8. H. Marchand, J. P. Ibbetson, P. T. Fini, X. H. Wu, S. Keller, S. P. Denbaars, J. S. Speck, and U.K.Mishra, *MRS Internet J. Nitride Semicond. Res.*, **4,** U462 (1999).
9. J. Park, A. Grudowski, C. J. Eiting, and R. D. Dupuis, *Appl. Phys. Lett.*, **73,** 333 (1998).
10. T. S. Zheleva, O.-H. Nam, M. D. Bremser, and R. F. Davis, *Appl. Phys. Lett.*, **71,** 2472 (1997).
11. S. Haffouz, B. Beaumont, and P. Gibart, *MRS Internet J. Nitride Semicond. Res.*, **3,** 1 (1998).
12. D. Marx, Z. Kawa, T. Nakayama, Y. Mihashi, T. Takami, M. Nunoshita, and T. Ozeki., *J. Cryst. Growth*, **189-190,** 87 (1998).
13. M. Gibbon, J. P. Stagg, C. G. Cureton, E. J. Thrush, C. J. Jones, R. E. Mallard, R. E. Pritchard, N. Collis, and A. Chew, *Semiconduct. Sci. Tech.*, **8,** 998 (1993).
14. T. Sasaki, M. Kitamura, and I. Mito, *J. Cryst. Growth*, **132**, 435 (1993).
15. O.-H. Nam, T. S. Zheleva, M. D. Bremser, and R. F. Davis, *J. Electron. Mater.*, **27,** 233 (1998).
16. H. Marchand, J. P. Ibbetson, P. T. Fini, X. H. Wu, S. Keller, S. P. Denbaars, J. S. Speck, and U.K.Mishra, *J. Cryst. Growth*, **195,** 328 (1998).
17. R. J. Shul, C. G. Willison, and L. Zhang, *SPIE*, **3511,** 252 (1998).
18. J. Wang, R. S. Q. Fareed, M. Hao, S. Mahanty, S. Tottori, Y. Ishikawa, T. Sugahara, Y. Morishima, K. Nishino, M. Osinski, and S. Sakai, *Journal of Applied Physics*, **85,** 1895 (1999).
19. T. Takeuchi, H. Amano, K. Hiramatsu, N. Sawaki, and I. Akasaki, *J. Cryst. Growth*, **115,** 634 (1991).
20. A. Watanabe, T. Takeuchi, K. Hirosawa, H. Amano, K. Hiramatsu, and I. Akasaki, *J. Cryst. Growth*, **128,** 391 (1993).

DISTRIBUTION:

1	MS 0601	R.M. Biefeld, 1126
1	MS 0601	C.C. Mitchell, 1126
1	MS 0885	D.B. Dimos, 1801
1	MS 1349	C.S. Ashley, 1846
1	MS 1349	J.C. Brinker, 1846
1	MS 9001	M. E. John, 8000
		Attn: J. Vitko, 8100, MS 9004
		D. R. Henson, 8200, MS 9007
		W. J. McLean, 8300, MS 9054
		P.N. Smith, 8500, MS 9002
		K. E. Washington, 8900, MS 9003
1	MS 9402	K.L. Wilson, 8703
1	MS 9405	R.H. Stulen, 8700
		Attn: J.M. Hruby, MS 9401
1	MS 9409	G.D. Kubiak, 8732
		Attn: J.E.M. Goldsmith, MS 9409
		W.C. Replogle, MS 9409
1	MS 9161	R.Q. Hwang, 8721
3	MS 9018	Central Technical Files, 8945-1
1	MS 0899	Technical Library, 9616
1	MS 9021	Classification Office, 8511/Technical Library,MS 0899, 9616
		DOE/OSTI via URL
1	MS 0188	D. Chavez, LDRD Office, 4001